



# Preferentially Engineering FeN<sub>4</sub> Edge Sites onto Graphitic Nanosheets for Highly Active and Durable Oxygen Electrocatalysis in Rechargeable Zn–Air Batteries

Meiling Xiao, Zihao Xing, Zhao Jin, Changpeng Liu, Junjie Ge, Jianbing Zhu,\* Ying Wang,\* Xiao Zhao,\* and Zhongwei Chen\*

Single-atom FeN<sub>4</sub> sites at the edges of carbon substrates are considered more active for oxygen electrocatalysis than those in plane; however, the conventional high-temperature pyrolysis process does not allow for precisely engineering the location of the active site down to atomic level. Enlightened by theoretical prediction, herein, a self-sacrificed templating approach is developed to obtain edge-enriched FeN<sub>4</sub> sites integrated in the highly graphitic nanosheet architecture. The *in situ* formed Fe clusters are intentionally introduced to catalyze the growth of graphitic carbon, induce porous structure formation, and most importantly, facilitate the preferential anchoring of FeN<sub>4</sub> to its close approximation. Due to these attributes, the as-resulted catalyst (denoted as Fe/N-G-SAC) demonstrates unprecedented catalytic activity and stability for the oxygen reduction reaction (ORR) and oxygen evolution reaction (OER) by showing an impressive half-wave potential of 0.89 V for the ORR and a small overpotential of 370 mV at 10 mA cm<sup>-2</sup> for the OER. Moreover, the Fe/N-G-SAC cathode displays encouraging performance in a rechargeable Zn–air battery prototype with a low charge–discharge voltage gap of 0.78 V and long-term cyclability for over 240 cycles, outperforming the noble metal benchmarks.

The rapid consumption of traditional fossil fuels and the accompanied global warming issues have impelled the development of clean, sustainable energy storage and conversion technologies.<sup>[1,2]</sup> Among the various candidates, rechargeable Zn–air batteries are recognized as the most promising energy

conversion system due to their high energy density, low cost, and zero emission.<sup>[3–6]</sup> However, the sluggish kinetics of the oxygen reduction reaction (ORR) and oxygen evolution reaction (OER) during the charge and discharge process result in high overpotential and low specific energy, thereby impeding the commercialization of Zn–air batteries.<sup>[7–12]</sup> Motivated by this challenge, great endeavors have been paid to exploit oxygen electrocatalysts with accelerated kinetics, with noble-metal-based materials known as the mainstream catalysts (Pt for ORR, Ir and Ru for OER). These catalysts, however, are only function actively to one of the two essential reactions, behave inactively to the other, and are criticized for their expensive and scarce nature. Therefore, developing cost-effective and efficient bifunctional oxygen electrocatalysts is regarded a cutting edge and essential research topic.<sup>[13–16]</sup>

The emergence of single-atom catalysts (SACs) is bringing out new opportunities to oxygen electrocatalysis. SACs based M-N-C with varied metal centers (M represents Fe, Co, Cu, Mn, Ni, Zn, etc.) have been explored as oxygen electrocatalysts.<sup>[17–24]</sup> Among them, single-atom Fe-N-C catalysts with FeN<sub>4</sub>

Dr. M. Xiao, Dr. Z. Jin, Prof. C. Liu, Prof. J. Ge, Dr. J. Zhu  
 State Key Laboratory of Electroanalytical Chemistry  
 Jilin Province Key Laboratory of Low Carbon Chemical Power  
 Changchun Institute of Applied Chemistry  
 Chinese Academy of Sciences  
 Changchun 130022, China  
 E-mail: zjb@ciac.ac.cn

Dr. M. Xiao, Dr. J. Zhu, Prof. Z. Chen  
 Department of Chemical Engineering  
 Waterloo Institute for Nanotechnology  
 Waterloo Institute for Sustainable Energy  
 University of Waterloo  
 Waterloo, Ontario N2L 3G1, Canada  
 E-mail: zhuchen@uwaterloo.ca

Dr. Z. Xing  
 Institute of Microscale Optoelectronics  
 Shenzhen University  
 Shenzhen 518060, China

The ORCID identification number(s) for the author(s) of this article can be found under <https://doi.org/10.1002/adma.202004900>.

DOI: 10.1002/adma.202004900

Dr. Z. Xing  
 Fachgebiet Angewante Nanophysik  
 Institut für Physik & IMN MacroNano@ (ZIK)  
 Technische Universität Ilmenau  
 Ilmenau 98693, Germany

Dr. Y. Wang  
 State Key Laboratory of Rare Earth Resource Utilization  
 Changchun Institute of Applied Chemistry  
 Chinese Academy of Sciences  
 Changchun 130022, China  
 E-mail: ywang\_2012@ciac.ac.cn

Dr. X. Zhao  
 Innovation Research Center for Fuel Cells  
 The University of Electro-Communications  
 Chofu, Tokyo 182-8585, Japan  
 E-mail: xiaozhao@uec.ac.jp

Dr. X. Zhao  
 State Key Laboratory of Automotive Simulation and Control  
 School of Materials Science and Engineering  
 Key Laboratory of Automobile Materials of MOE  
 Jilin University  
 Changchun 130012, China

coordination structure as operational active site are hailed as the most promising candidate due to the more suitable binding strength for oxygen-containing intermediates.<sup>[25–30]</sup> The past decades have witnessed the transition in the development of Fe-N-C catalysts from the trial-and-error experiment to the in-depth understanding on the structural–activity relationship. The new knowledge gained is beneficial toward rational design of high-performance Fe-N-C catalysts that can compete with noble metal benchmarks. For instance, the local carbon structure surrounding FeN<sub>4</sub> moiety is found to play a key role in determining the final catalytic properties, with FeN<sub>4</sub> located at the edge superior to the one in plane.<sup>[31]</sup> In this regard, preferential construction of edge sites constitutes an appealing approach to further improve the catalytic activity of Fe-N-C catalysts toward their real-world implementation. Nevertheless, the graphitizing degree of carbon is usually poor in the conventional edge site dominant samples, thus resulting in inferior electrochemical stability, especially in the harsh OER process, where only highly graphitic carbon nanotubes and graphene can survive the long-term operation.<sup>[32–34]</sup> To this end, integrating the more favorable FeN<sub>4</sub> edge sites into a highly graphitic carbon substrate is urgently imperative to realize the practical application in rechargeable Zn–air battery.

Enlightened by the theoretical prediction, herein we report a novel self-sacrificed templating approach to preferentially integrating FeN<sub>4</sub> edge sites into the highly graphitic few-layer graphene (Fe/N-G-SAC). In sharp contrast with the conventional synthetic procedure where trace amount of iron precursors is necessary, this strategy utilized extremely excessive iron precursors. The in situ generated Fe clusters not only enable a highly graphitic structure, but also facilitate the preferential deposition of FeN<sub>4</sub> moieties adjacent to iron clusters, such that the post etching of the inactive iron clusters leads to formation of the desirable FeN<sub>4</sub> edge sites. Meanwhile, rich mesopores were created, benefiting the mass/electron transportation and thereby promoting the reaction kinetics. Due to these structural attributes, the as-prepared Fe/N-G-SAC exhibited admirable catalytic and stability for both ORR and OER, outperforming the benchmark Pt/C and Ir/C catalysts. Notably, the decreased charge/discharge gap and long-term stability in a homemade Zn–air battery further revealed the superiority of the Fe/N-G-SAC as bifunctional oxygen catalysts. These interesting findings will offer a new pathway toward efficient and durable oxygen electrocatalysis and high-performance Zn–air battery.

We first carried out density functional theory (DFT) calculations to investigate the feasibility of the Fe-template strategy for the preferential synthesis of edge-enriched Fe-N<sub>4</sub> site. Several typical isomers of Fe cluster anchored on Fe-N<sub>4</sub> moiety doped graphene with various distances between Fe cluster and Fe-N<sub>4</sub> moiety was constructed. The relative formation energy ( $E_f$ ) was systematically compared in Figure 1a–d. Clearly, the configuration with Fe cluster and Fe-N<sub>4</sub> (Fe cluster/Fe-N<sub>4</sub>-1) in the nearest approximation exhibits the lowest  $E_f$  of -21.19 eV, due to the stabilization feature of FeN<sub>4</sub> by Fe clusters. Thus, we anticipate that by introducing excessive Fe cluster during synthesis, the energetically preferred Fe cluster/Fe-N<sub>4</sub>-1 structure will dominate in the sample, and finally lead to the formation of the edge dominant FeN<sub>4</sub> sites in the sample after the removal of Fe clusters. We then calculated the configuration advantages of the edge site

over the in-plane one, starting from the charge density difference diagrams (Figure 1e,f). A clear charge redistribution occurs in the Fe-N<sub>4</sub> edge site, due to the reduced coordination number of edge N (N-C coordination number = 1) in comparison to the in-plane sites (N-C coordination number = 2). The electron withdrawn feature of N thus leads to an increased electron transfer from Fe atom to the nearby N atom in the FeN<sub>4</sub> edge sites. The intensified electron transfer was further validated by the higher Bader charge estimated on the edge site (1.17 e vs 0.97 e for in-plane site). It should be also noted that a significant spin polarization is observed in the edge site (Figure 1g,h), which is considered favorable for boosting oxygen electrocatalysis.<sup>[35,36]</sup> The regulated electronic configuration on the edge site promisingly modifies adsorption–desorption behaviors of oxygen-containing intermediates. The partial density of states (DOS) of Fe were calculated to gain more information on the Fe-3d electronic configuration. The negative shift of the d-band center on the edge FeN<sub>4</sub> site (-2.99 eV vs -1.78 eV for in-plane FeN<sub>4</sub>) implies a weakened binding strength of adsorbates on the edge site (Figure S1, Supporting Information). As is known, the rate-determining step on the in-plane Fe-N<sub>4</sub> site is the last electron transfer step, i.e., the OH desorption, suggesting that weakening Fe–O affinity is imperative for activity enhancement. We therefore systematically investigated the adsorption–desorption properties on these two sites. Excitingly, the adsorption free energy of OH\* ( $\Delta G_{OH^*}$ ) on edge site (0.94 eV) was higher than that on in-plane site (0.36 eV), revealing a faster OH desorption process on the former (Figure 1i). The Gibbs free energy diagrams at  $U = 1.23$  V (Figure S2, Supporting Information) confirms the extremely strong adsorption of OH\* on the in-plane Fe-N<sub>4</sub> site results in a larger energy barrier of 0.87 eV for the last electron transfer step, whereas the well-regulated OH\* binding strength on the edge site leads to significantly decreased energy barrier of 0.29 eV, implying improved intrinsic activity. Theoretical ORR overpotential on these two sites was estimated for an intuitive comparison. Impressively, edge site shows a fairly low overpotential of 0.29 V, while this value turns out to be 0.87 V for the in-plane site, verifying the superiority of the edge site in ORR catalysis (Figure S3, Supporting Information). Beyond that, edge site also demonstrates superior OER activity by showing decreased energy barrier (1.71 eV vs 2.18 eV on in-plane site) for the rate-determining step ( $O^* + H_2O \rightarrow OOH^* + H^+ + e^-$ ), as shown in the OER Gibbs free energy diagrams (Figure 1j).

Guided by the DFT prediction, single-atom Fe-N<sub>x</sub>-C catalysts with enriched edge site was prepared in the proposed self-sacrificed strategy as illustrated in Figure 2a. Specifically, 1,8-diaminonaphthalene (DAN) was polymerized first using FeCl<sub>3</sub> as oxidation initiator to obtain poly-1,8-diaminonaphthalene (PDAN) as precursor. The initial mass ratio of DAN/FeCl<sub>3</sub> was found crucial to determine the structure of the polymerized product as the morphology of PDAN varies from microsphere-assembled nanosheet/microspheres aggregates to uniform microspheres with decreasing the ratio from 5/1, 1/1, 1/10 to 1/20 (Figure S4, Supporting Information). And the ratio of 1/10 is demonstrated critical to enable a uniform structure. Subsequently, the resultant PDAN precursor was pyrolyzed under following N<sub>2</sub> atmosphere and underwent acidic leaching treatment to remove the unstable Fe species that are adjacent to single-atom Fe sites, the derived catalyst was denoted

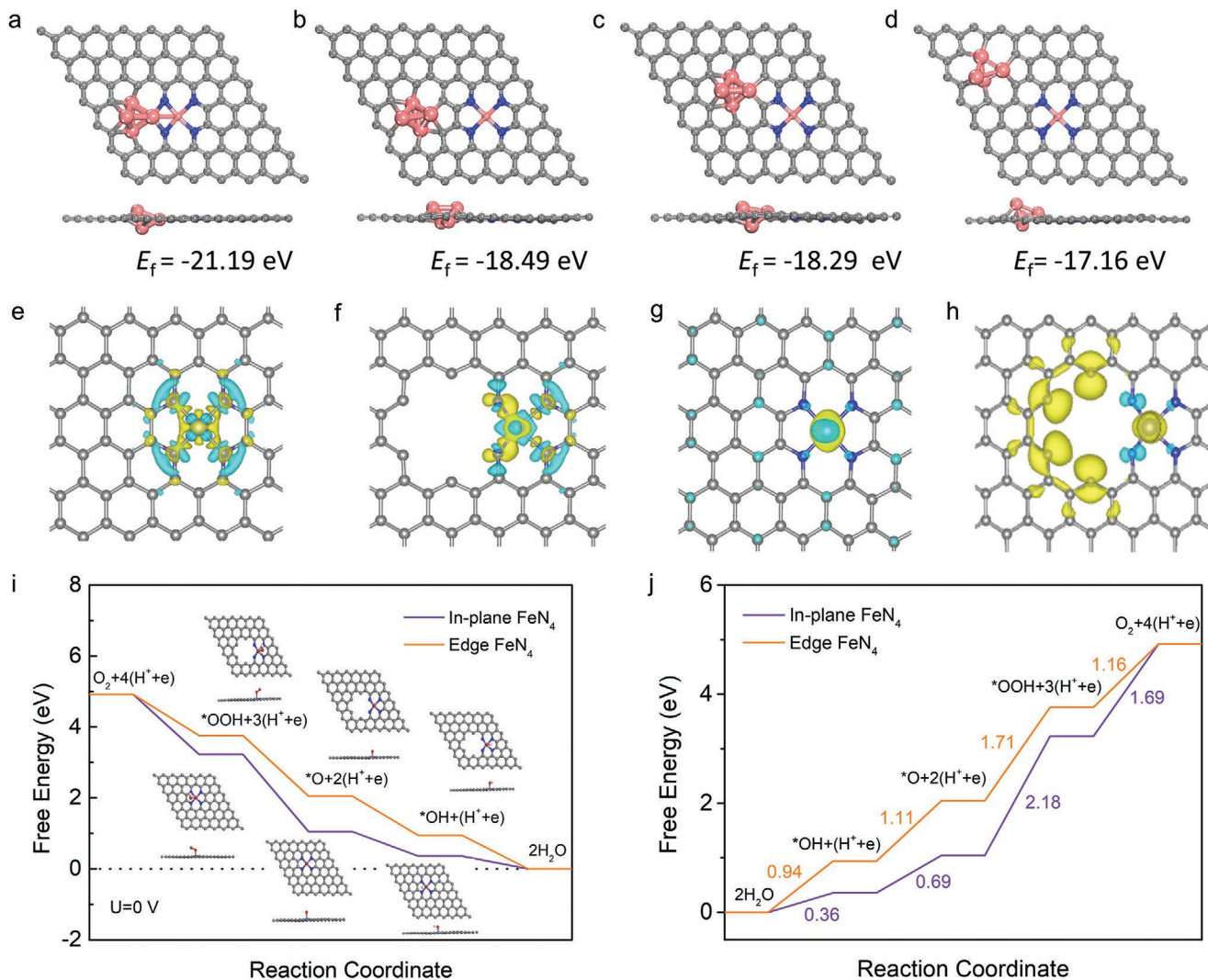


**Figure 1.** a-d) Various Fe cluster/Fe-N<sub>4</sub> site configurations and the corresponding formation energy ( $E_f$ ). e,f) Charge density difference. g,h) Spin density. i) ORR and j) OER Gibbs free energy diagrams on the edge and in-plane sites.

as Fe/N-G-SAC (DAN/FeCl<sub>3</sub> ratio is 1/10). In this process, the excessive amount of Fe not only promotes the graphitic carbon formation, but also serves as self-scarified template to yield edge-rich single-atom Fe sites in the pyrolyzed material. For comparative study, the precursors with DAN/FeCl<sub>3</sub> mass ratio of 5/1, 1/1, and 1/20 were subject to the same procedure and the resultant catalysts were denoted as Fe/N-C-0.2, Fe/N-C-1, and Fe/N-C-20, respectively. In addition, Fe-free nitrogen-doped carbon (N-C) was also synthesized using PDAN polymerized by ammonium persulfate ((NH<sub>4</sub>)<sub>2</sub>S<sub>2</sub>O<sub>8</sub>) as precursor.

The morphology of the pyrolyzed materials was monitored by scanning electron microscopy (SEM) and transmission electron microscopy (TEM). The representative SEM images of Fe/N-G-SAC revealed that the uniform polymer microspheres with 250 nm (Figure S4c, Supporting Information) convert to porous foam structure upon the pyrolysis (Figure 2b). The foam structure is assembled by the graphene-like nanosheets, which turn out to be wrinkled on the edges (Figure 2c). High-resolution transmission electron microscopy (HRTEM) image

(Figure 2d) clearly show graphene sheet with an average thickness of about 2 nm, corresponding to few-layer graphene. The lattice fringe of the as-prepared few-layer graphene was estimated to be 0.35 nm (Figure 2d), larger than the value of graphite (0.335 nm), probably due to the substitution of larger heteroatoms (N and/or Fe). The well-defined diffraction spots and rings in the selected area electron diffraction (SAED) pattern (Figure 2e) further confirm the high graphitic degree of the carbon substrate as a result of Fe-assisted catalytic growth of carbon. Although massive amount of Fe was utilized, no iron particles can be observed in whole region of the randomly selected TEM image, which suggests the crystalline Fe species were completely removed after acidic leaching. However, the presence of Fe residuals was confirmed by scanning transmission electron microscopy (STEM) elemental mapping, where Fe and N elements were homogeneously distributed in the graphene sheets (Figure 2f). Besides, the ICP results also verified its existence with a content of 0.67 wt%, therefore, we believe that the trace remaining Fe may exist in

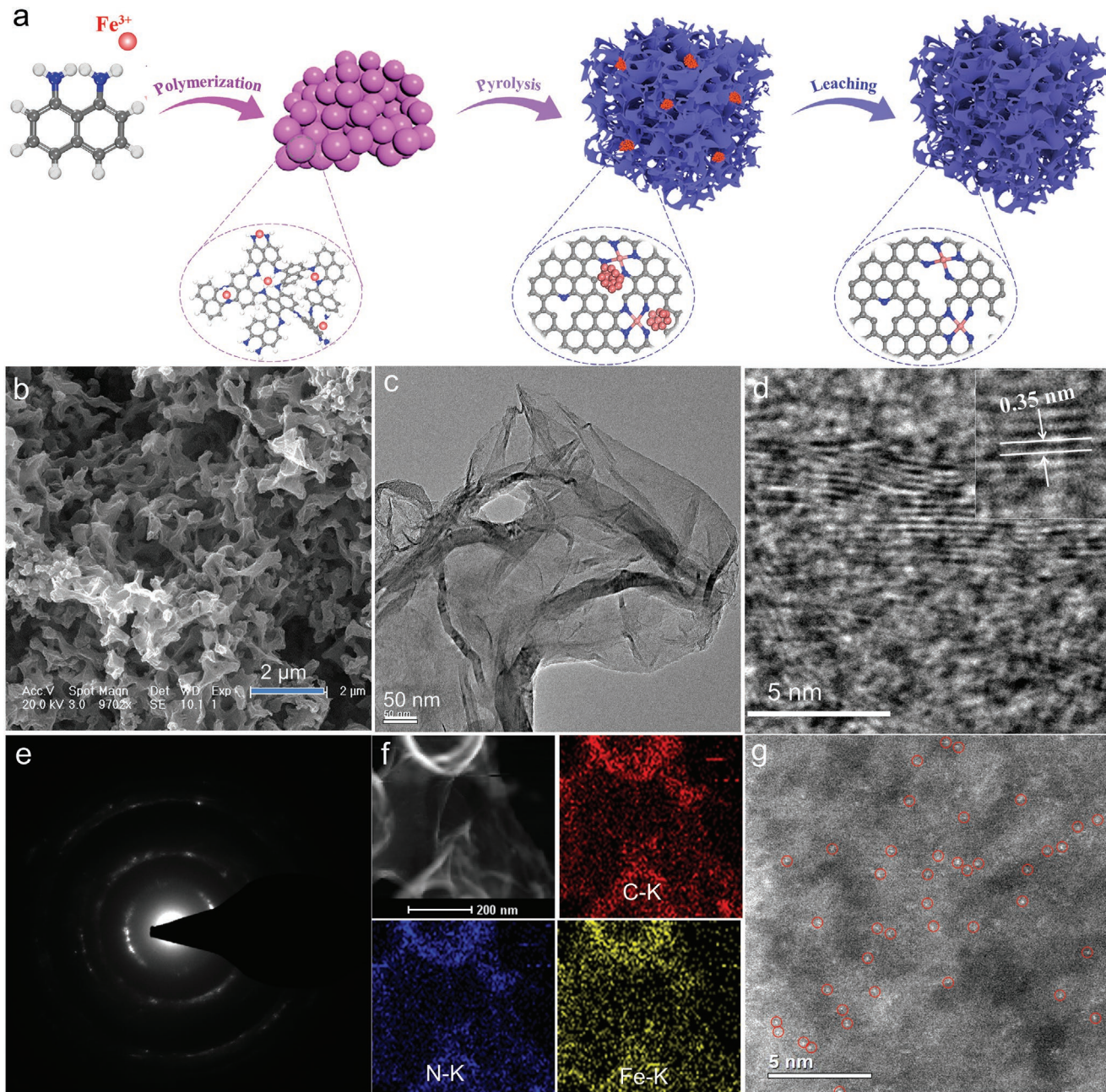


**Figure 2.** a) Illustration of the preparation of Fe/N-G-SAC. b) SEM, c) TEM, d) HRTEM, e) SAED, f) HAADF-STEM and EDS mapping images (C red, N blue, Fe yellow), and g) aberration-corrected HAADF-STEM of the isolated Fe atoms involved Fe/N-G-SAC catalyst.

the form of atomic Fe-N<sub>x</sub> coordinates. To discern the atomic structure of Fe/N-G-SAC, sub-angstrom resolution aberration-corrected HAADF-STEM was used. Several single bright dots can be clearly distinguished from the nitrogen doped carbon matrix, which are attributable to isolated Fe atoms according to their Z-contrast (Figure 2g). By contrast, Fe/N-C-0.2, Fe/N-C-1 exhibits distinct different structures from Fe/N-G-SAC, in which bulk aggregates or nanospheres featured with Fe nanoparticles encapsulated into graphitic layer sub-unites are formed, while Fe/N-C-20 share the similar morphology and microstructure as the Fe/N-G-SAC (Figure S5, Supporting

Information). The morphology of N-C was also checked, revealing amorphous carbon nanosphere structure (Figure S6, Supporting Information). These results imply the key role of excessive amount of Fe in enabling edge-rich single-atom FeN<sub>x</sub> site and high graphitic degree of carbon substrate.

The highly graphitic features of the carbonized catalysts were further validated by X-ray diffraction (XRD) and Raman spectroscopy. XRD pattern of Fe/N-G-SAC exhibits remarkable peak at  $2\theta = 26.5$  ascribing to (002) diffraction of graphitic carbons (Figure S7, Supporting Information). Its intensity was found to decrease with increasing DAN/FeCl<sub>3</sub> ratio, suggesting

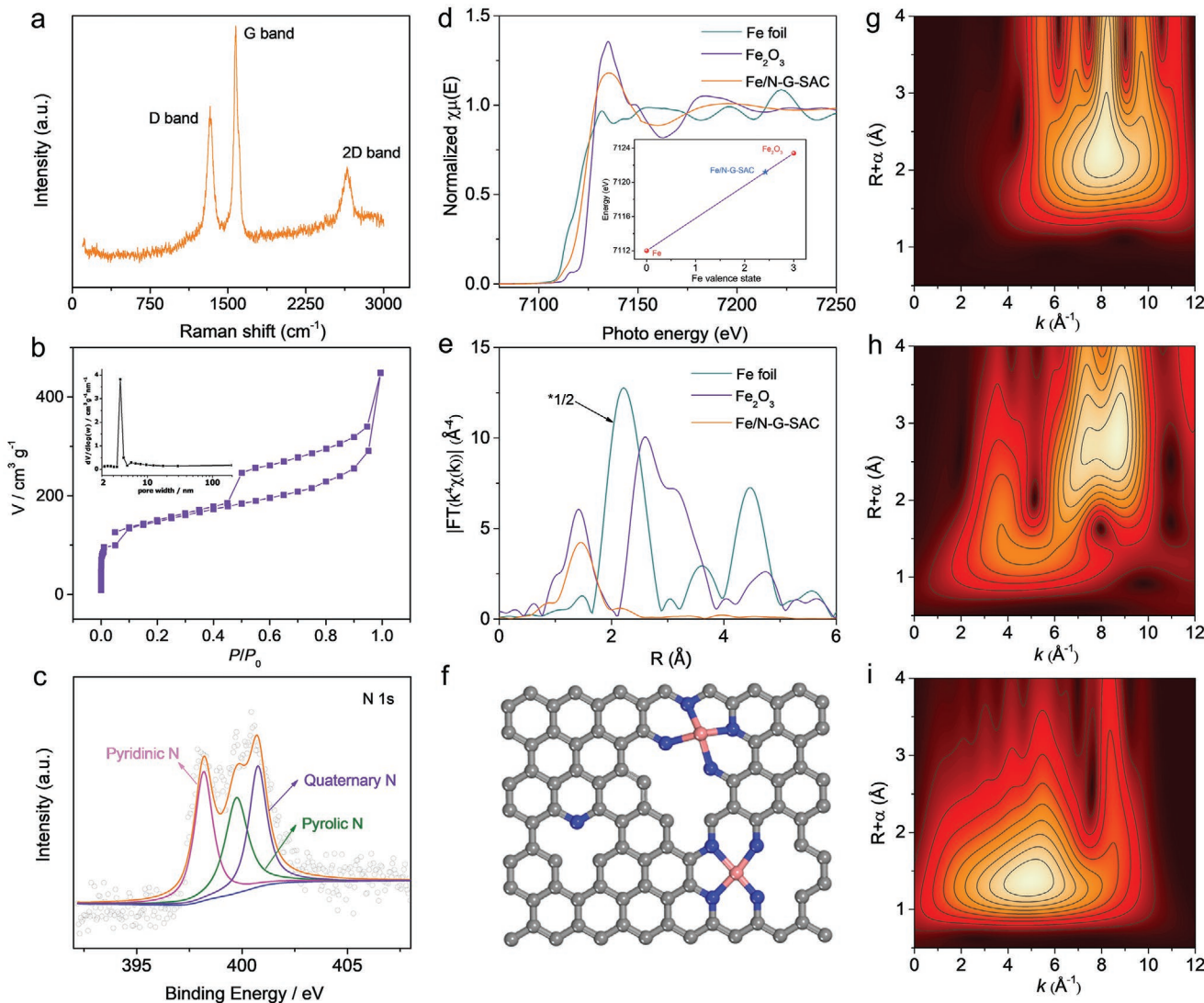


**Figure 3.** a) Raman spectrum. b)  $N_2$  adsorption–desorption isotherm, inset is the corresponding pore size distribution curve. c) High-resolution N 1s XPS of Fe/N-G-SAC. d) XANES of Fe K-edge, inset is linear fitting curve of Fe/N-G-SAC, Fe foil and  $Fe_2O_3$  derived from corresponding Fe K-edge XANES spectra. e) Fourier transforms of  $k^3$ -weighted Fe K-edge EXAFS data. f) Schematic structure for Fe/N-G-SAC. g–i) Wavelet transforms for the  $k^3$ -weighted Fe K-edge EXAFS signals of Fe foil (g),  $Fe_2O_3$  (h) and Fe/N-G-SAC (i).

the vital role of Fe in catalyzing graphitic carbon growth. This is in line with the increased ratio of D band to G band ( $I_D/I_G$ ) observed in Raman spectra (Figure S8, Supporting Information). It should be noted that the characteristic 2D band of graphene material was present in the Fe/N-G-SAC (Figure 3a), in consistent with the graphene structure observed in the TEM images. The well-graphitic structure of graphene not only facilitates electron transfer during electrochemical reaction process, but also enables the good electrocatalytic stability during the harsh OER process. As we mentioned above, the in situ generated Fe nanoparticles that promote graphitic degree were easily dissolved to induce rich porous structure and thus promote the exposure of adjacent single-atom site. On this basis, the pore structure and surface area were examined by nitrogen-adsorption–desorption technique. Isotherm of Fe/N-G-SAC showed a hysteresis loop at a relative pressure  $P/P_0$  of 0.4–1 with

a surface area of  $530\text{ m}^2\text{ g}^{-1}$ , corresponding to type-IV isotherm characteristics for mesoporous materials (Figure 3b). The pore size distribution analysis further confirmed the mesoporous structure with average pore size of 3.8 nm. The higher BET surface area (Figure S9 and Table S1, Supporting Information), which was benefited from 3D interconnected porous structure combined with rich mesopores, was favorable for active site exposure and mass transfer during the electrochemical process, thereby superior catalytic activity was expected on Fe/N-G-SAC.

The surface composition and electronic structure of the as-prepared catalysts were probed by X-ray photoelectron spectroscopy (XPS). XPS survey spectra shows the presence of C, O, N elements (Figure S10, Supporting Information). The successful N doping into the carbon matrix is further confirmed by the appearance of a typical C–N peak (287.2 eV) in the high-resolution C 1s XPS spectra (Figure S11, Supporting

Information), which not only serves as anchoring sites for metal atoms deposition, but also tailors the charge/spin density of adjacent carbon atoms to generate active sites for oxygen electrocatalysis. Specifically, C–N relative content shows a downward trend with increasing Fe portion, implying the critical role of Fe in modulating defective carbon configurations for active site deposition (Figure S12, Supporting Information). The chemical binding states of N was then carefully examined. Three peaks, located at 398.1, 398.9, and 400.8 eV, can be observed in the high-resolution N 1s spectra, which are corresponding pyridinic N, pyrrolic N and graphitic N, respectively (Figure 3c and Figure S13a–c, Supporting Information). Among these N species, pyridinic N are regarded responsible for the formation of single-atom Fe-N<sub>x</sub> site, therefore the higher content with increasing Fe portion contributed to the homogeneous single-atom Fe-N<sub>x</sub> moiety without any Fe clusters/particles (Figure S13d, Supporting Information). Unfortunately, no obvious Fe signal can be detected because of the coverage of graphitic layers on the Fe<sub>3</sub>C surface and/or the content of Fe is lower than the detection limit (Figure S14, Supporting Information). In order to monitor the chemical state of Fe, X-ray absorption near edge structure (XANES) spectroscopy was employed. The Fe K-edge XANES spectra demonstrate that the energy absorption threshold of Fe/N-G-XAS locates between that of Fe foil and Fe<sub>2</sub>O<sub>3</sub>, indicating the valence state of Fe species in Fe/N-G-SAC sample is between 0 and +3 (Figure 3d). This observation is also in line with the moderate white-line intensity of Fe/N-G-SAC compared with that of Fe foil and Fe<sub>2</sub>O<sub>3</sub>. Further information on the Fe valence state was obtained by employing the linear combination method, where the edge absorption energy of the standard samples was plotted with their valence state. As shown in the inset of Figure 3d, the Fe valence state of Fe/N-G-SAC was estimated to be 2.4. The coordination configuration of isolated Fe atoms in Fe/N-G-SAC was examined by extended X-ray absorption fine structure (EXAFS) spectroscopy. The Fourier transform (FT) k<sup>3</sup>-weighted Fe K-edge EXAFS spectrum of the Fe/N-G-SAC displays a main peak at  $\approx$ 1.5 Å, which is assigned to Fe–N scattering path (Figure 3e). In contrast to Fe foil and Fe<sub>2</sub>O<sub>3</sub>, the absence of metallic Fe–Fe path (2.2 Å) in the spectrum of Fe/N-G-SAC further verifies the atomic dispersion of Fe species. Quantitative EXAFS fitting analysis reveals that the isolated Fe atom is coordinated by four N atoms with Fe–N bond length of 1.99 Å, forming a Fe-N<sub>4</sub> configuration (Figure 3f; Figure S15 and Table S2, Supporting Information). Wavelet transform (WT) of Fe K-edge EXAFS oscillations that can provide both radial distance and k-space resolution was also performed for further confirmation of atomic isolation of Fe atoms in the Fe/N-G-SAC. In line with the FT-EXAFS analysis, the WT contour plot of Fe/N-G exhibits only one intensity maximum at 5 Å<sup>-1</sup>, which is assigned to Fe–N bond (Figure 3i). By contrast, both Fe foil and Fe<sub>2</sub>O<sub>3</sub> counterparts show a higher intensity maximum at  $\approx$ 8.2 Å<sup>-1</sup>, corresponding to metallic Fe–Fe scattering (Figure 3g,h). The combined FT- and WT-EXAFS results well certifies the atomically dispersed Fe-N<sub>4</sub> configuration, which is commonly regarded as the most efficient active site for oxygen electrocatalysis among the reported single-atom sites.

We then evaluated the electrocatalytic properties of the Fe/N-G-SAC in 0.1 M KOH electrolyte by rotating disk electrode (RDE) and rotating ring disk electrode (RRDE) methods, with the commercial Pt/C and Ir/C utilized as the ORR and OER benchmarks, respectively. The mass loading for the Pt/C (20 wt%, Johnson Matthey) and the non-precious metal catalysts was 0.1 (corresponding to 20 µg<sub>Pt</sub> cm<sup>-2</sup>) and 0.6 mg cm<sup>-2</sup>, respectively. The structure advantage of Fe/N-G-SAC over other samples with Fe particles encapsulated in carbon layer was confirmed in Figure 4a, in which the most positive half-wave potential was observed on Fe/N-G-SAC electrode of 0.89 V, even better than the commercial Pt/C-JM catalyst and superior to those of most recently reported non-precious metal catalysts.<sup>[28,37–41]</sup> The superb ORR activity of Fe/N-G-SAC catalyst over the reference samples was also revealed by the comparison of kinetic currents at fixed potentials (Figure 4b). Specifically, at 0.9 V, the Fe/N-G-SAC delivered a kinetic activity of 3.837 mA cm<sup>-2</sup>, surpassing those of the Fe/N-C-0.2 (0.287 mA cm<sup>-2</sup>), Fe/N-C-1 (0.459 mA cm<sup>-2</sup>), and Pt/C (2.395 mA cm<sup>-2</sup>). It is noted that the Fe/N-G-SAC also outperformed Fe/N-C-20 although they shared the similar graphene sheet structure. The enhanced ORR performance may be caused by the following two factors. First, the Fe content detected in the Fe/N-G-SAC was higher than that in the Fe/N-C-20, suggesting increased active site density of the former. Second, as nitrogen-adsorption–desorption isotherms revealed, enlarged surface area was achieved on Fe/N-G-SAC, which was beneficial for the accessibility of active sites and facilitated transportation of reactants/intermediates/product. Besides, the Fe/N-G-SAC exhibits a smaller Tafel slope of 50 mV dec<sup>-1</sup> than the other Fe-based counterparts, demonstrating the faster kinetics of ORR on Fe/N-G-SAC (Figure 4d). Apart from superior activity, enhanced selectivity was observed on the Fe/N-G-SAC using RRDE method and Koutecký–Levich (K–L) equation, revealing less than 3% H<sub>2</sub>O<sub>2</sub> yield and 4-electron transfer pathway (Figure 4a,c and Figures S16–S19, Supporting Information).

To fulfill the requirement of bifunctional oxygen cathodes for rechargeable Zn-air batteries, the OER catalytic activity was also assessed in 0.1 M KOH at 1600 rpm. Figure 4e shows a dependence of OER activity on nanostructure, among which Fe/N-G-SAC exhibited the highest OER activity with a lowest E<sub>j=10</sub> (potential to reach a current density of 10 mA cm<sup>-2</sup>) of 1.60 V. Moreover, the lowest Tafel slope of 73 mV dec<sup>-1</sup> (Figure 4f) was observed on Fe/N-G-SAC, validating the accelerated OER kinetics. The bifunctional activity is evaluated by the potential difference between E<sub>1/2</sub> for ORR and E<sub>j=10</sub> for OER (Figure 4g,h), a smaller value of ΔE (ΔE = E<sub>j=10</sub> - E<sub>1/2</sub>) indicates superior bifunctionality. Intriguingly, a small ΔE as low as 0.71 V was discerned in the Fe/N-G-SAC, lower than those of other counterparts (e.g., Fe/N-C-0.2, 0.841 V, Fe/N-C-1, 0.804 V, and Fe/N-C-20, 0.754 V), and outperforming the commercial noble metal catalysts (0.756 V). Besides, the bifunctionality of the as-prepared Fe/N-G-SAC is also superior to most of the recently reported NPMCs<sup>[42–47]</sup> (Figure 4i). The intrinsically exceptional activity of single-atom Fe-N<sub>4</sub> site, strong coupling effect between active sites and substrate, and improved accessibility throughout the 3D mesoporous graphene nanosheets synergistically boost the bifunctional electrocatalytic performance, making Fe/N-G-SAC promising candidate to replace noble-metal materials for next-generation energy conversion and storage.

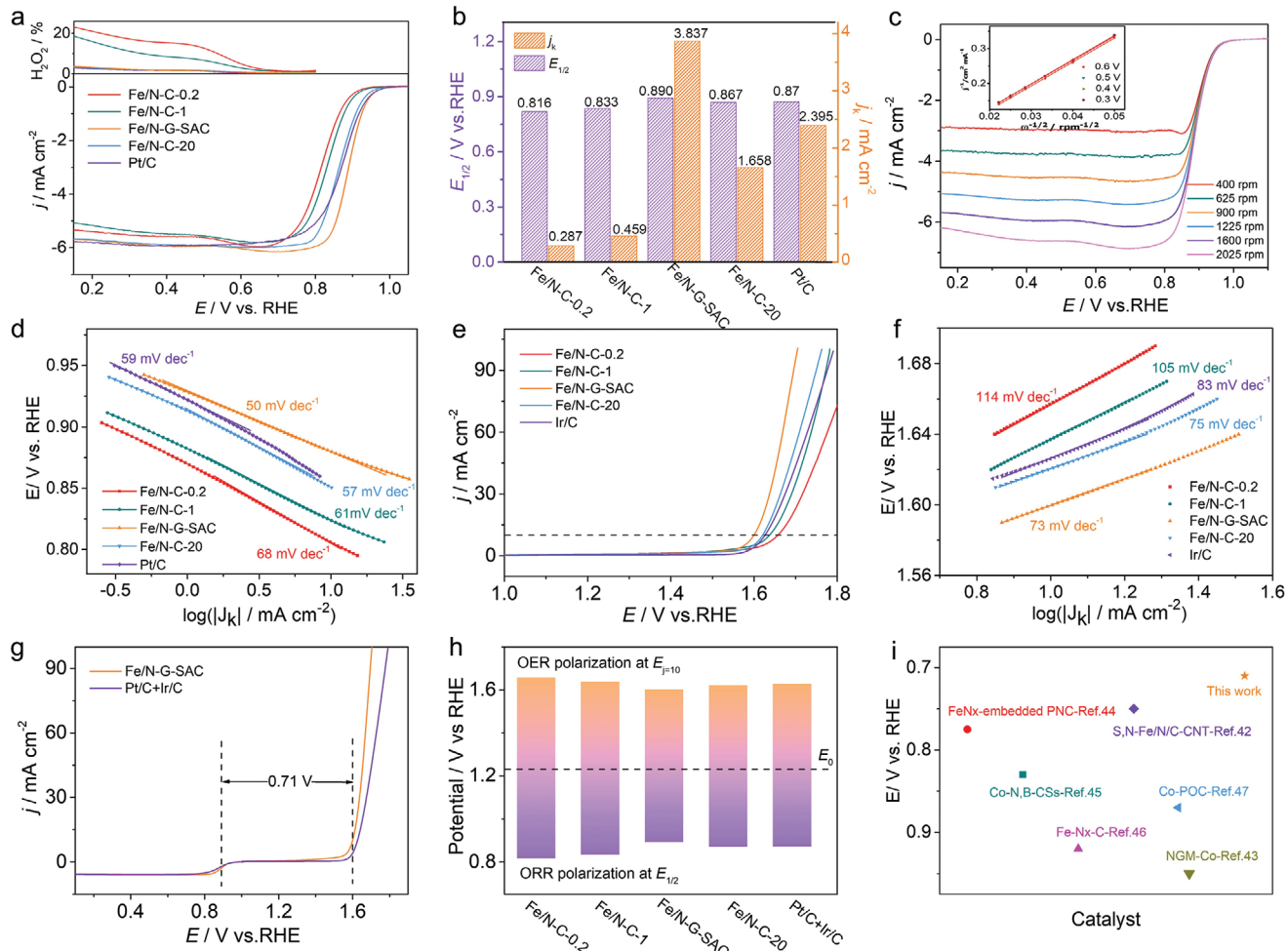


**Figure 4.** a) ORR polarization curves of the as-prepared catalysts and the commercial Pt/C. b) Summary of half-wave potential ( $E_{1/2}$ ) and kinetic current density ( $J_k$ ) at 0.9 V. c) ORR polarization curves of Fe/N-G-SAC at different rotating speeds, inset is the K-L plots. d) Tafel slopes for ORR. e) The OER polarization curves of all samples. f) Tafel plots for OER. g) The entire LSV curves for bifunctional activities within the ORR and OER potential window of Fe/N-G-SAC, Pt/C and Ir/C at 1600 rpm. h) Potential differences between the  $E_{1/2}$  of ORR and  $E_{j=10}$  of OER for the as-prepared catalysts and i) potential difference comparisons between Fe/N-G-SAC and other recently reported single-atom catalysts.

Furthermore, as one of the important criterions to estimate the application prospects of an electrocatalyst, stability was investigated using accelerated durability test (ADT). The ADT results conducted in ORR potential window showed that after 10 000 cycles, the half-wave potential for Fe/N-G-SAC only underwent a slight negative shift of 3 mV, which is much smaller than that for Pt/C catalyst of 13 mV (Figure S20, Supporting Information). The dramatically improved stability was attributable to the decreased  $\text{H}_2\text{O}_2$  yield that can mitigates poisoning oxygen radicals formation<sup>[48,49]</sup> and the excellent anti-corrosion character of highly graphitic carbon support. While for OER, superior stability was also obtained on Fe/N-G-SAC with only 6 mV positive shift in  $E_{j=10}$  after 2000 continuous cycling (Figure S21, Supporting Information). The distinguished stability in the harsh OER condition was ascribable to the highly ordered graphitic carbon structure, and strong interaction between active sites and support, which suppressed electrochemical corrosion of carbon substrate and detachment of single-atom Fe-N<sub>4</sub> sites from graphene support. The

inferior OER stability of the Ir/C benchmark is probably due to the severe carbon corrosion and the Ostwald ripening of Ir nanoparticles.

The outstanding bifunctional activity and stability of Fe/N-G-SAC greatly stimulates us to explore its practical application in Zn-air batteries, and a homemade rechargeable Zn-air battery with Fe/N-G-SAC as cathode was assembled (Figure 5a). The commercial noble metal catalysts (Pt/C + Ir/C) were also integrated into a Zn-air battery for comparison. As illustrated in the charge-discharge polarization curves (Figure 5b), a much higher discharge current density and a slightly lower charge-discharge voltage gap are obtained on Zn-air battery catalyzed by Fe/N-G-SAC battery compared to that of Pt/C + Ir/C, manifesting superior activity and improved rechargeability of the battery. Furthermore, higher maximum power density was delivered by Fe/N-G-SAC battery ( $120 \text{ mW cm}^{-2}$ , Figure 5c), far exceeding that of Pt/C + Ir/C ( $81 \text{ mW cm}^{-2}$ ). The long-term durability was then investigated by galvanostatic charge-discharge at a constant current density

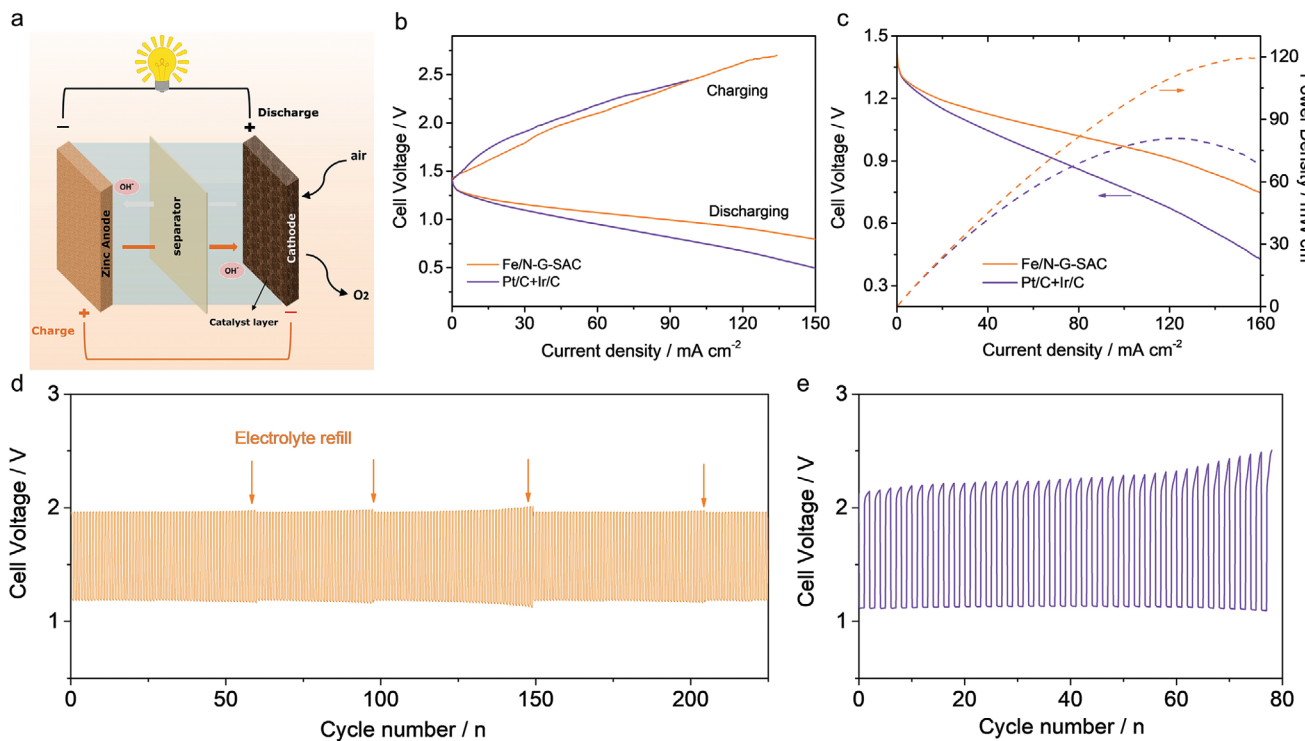


**Figure 5.** a) Schematically depicts the structure of assembled rechargeable Zn–air batteries. b,c) Polarization and power density curves of the liquid ZABs using Fe/N-G-SAC or Ir/C+20% Pt/C catalysts. d,e) Charge and discharge polarization curves of the ZABs using Fe/N-G-SAC (d) and Ir/C+20% Pt/C (e) catalysts as the air cathode.

of 10 mA cm<sup>-2</sup>. As shown in Figure 5d, Fe/N-G-SAC battery generates a narrower charge–discharge gap of 0.78 V initially, after 240 cycles, there is no obvious voltage fading, demonstrating the excellent durability. On the contrary, the battery with Pt/C + Ir/C as cathode presented limited cyclability of less than 78 cycles. These results reveal that Fe/N-G-SAC is a promising catalyst for the rechargeable Zn–air battery application. Notably, the stability achieved on the Fe/N-G-SAC was the highest among the reported SACs for Zn–air batteries thus far,<sup>[42–44,46]</sup> further confirming the superiority of the well-designed integrative configuration and highly graphitic carbon structure.

Inspired by the superior ORR and OER performance of the Fe/N-G/SAC, we further investigated its potential application in a reversible H<sub>2</sub>–O<sub>2</sub> fuel cell. Impressively, the fuel cell with Fe/N-G-SAC as cathode exhibits higher open circuit voltage than the cell with Pt/C+Ir/C (Figure S22a, Supporting Information). Besides, it can deliver a maximum power density of 179 mW cm<sup>-2</sup>, outperforming the noble metal benchmark (140 mW cm<sup>-2</sup>), demonstrating the higher ORR activity of Fe/N-G-SAC. Beyond that, the water electrolysis with Fe/N-G-SAC as anode also shows improved activity than that of Pt/C+Ir/C (Figure S22b, Supporting Information). These results reveal the great promise of Fe/N-G-SAC as oxygen electrode in the reversible H<sub>2</sub>–O<sub>2</sub> fuel cell.

In summary, we successfully developed a facile and potentially scalable strategy for the synthesis of single-atom FeN<sub>4</sub> edge-sites dominated graphene sheet, which show great promise as oxygen electrode in Zn–air batteries. By combining

the DFT calculations and the experimental investigations, the superiority of the catalysts structure is confirmed. While the edge dominated FeN<sub>4</sub> sites confer the catalysts with extraordinary activity due to optimized adsorption behavior, the graphitic carbon structure endows the catalysts with superb stability under harsh OER condition. In a home-made Zn–air battery, the Fe/N-G-SAC electrode delivers a narrow charge–discharge gap of 0.78 V as well as a nearly unfading activity after 240 cycles. Our finding is of great significance to the development of nanostructured carbon-based alternatives to noble metal catalysts.

## Supporting Information

Supporting Information is available from the Wiley Online Library or from the author.

## Acknowledgements

M.X. and Z.X. contributed equally to this work. The work was supported by the National Science and Technology Major Project (2016YFB0101202), National Natural Science Foundation of China (21633008, 1875243, 21673220, U1601211), Jilin Province Science and Technology Development Program (20190201270JC, 20180101030JC). The authors also acknowledge the support provided by the Natural Sciences and Engineering Research Council of Canada (NSERC), University of Waterloo, Waterloo Institute for Nanotechnology. Part of the computational time is supported by the High Performance Computing Center of Jilin University and Jilin Province, as well as Network and Computing Center of Changchun Institute of Applied Chemistry.

## Conflict of Interest

The authors declare no conflict of interest.

## Keywords

bifunctional oxygen electrocatalysts, edge sites, single-atom catalysts, stability, Zn-air batteries

Received: July 18, 2020

Revised: October 2, 2020

Published online:

- [1] J. Luo, J.-H. Im, M. T. Mayer, M. Schreier, M. K. Nazeeruddin, N.-G. Park, S. D. Tilley, H. J. Fan, M. Grätzel, *Science* **2014**, *345*, 1593.
- [2] Z. P. Cano, D. Banham, S. Ye, A. Hintennach, J. Lu, M. Fowler, Z. Chen, *Nat. Energy* **2018**, *3*, 279.
- [3] J. S. Lee, S. T. Kim, R. Cao, N. S. Choi, M. Liu, K. T. Lee, J. Cho, *Adv. Energy Mater.* **2011**, *1*, 34.
- [4] G. Li, X. Wang, J. Fu, J. Li, M. G. Park, Y. Zhang, G. Lui, Z. Chen, *Angew. Chem., Int. Ed.* **2016**, *55*, 4977.
- [5] J. Fu, Z. P. Cano, M. G. Park, A. Yu, M. Fowler, Z. Chen, *Adv. Mater.* **2017**, *29*, 1604685.
- [6] Y.-P. Deng, Y. Jiang, R. Liang, S.-J. Zhang, D. Luo, Y. Hu, X. Wang, J.-T. Li, A. Yu, Z. Chen, *Nat. Commun.* **2020**, *11*, 1952.
- [7] Z. W. Seh, J. Kibsgaard, C. F. Dickens, I. Chorkendorff, J. K. Nørskov, T. F. Jaramillo, *Science* **2017**, *355*, eaad4998.
- [8] Y. Xu, Y. Zhang, Z. Guo, J. Ren, Y. Wang, H. Peng, *Angew. Chem.* **2015**, *127*, 15610.
- [9] J. Zhu, M. Xiao, Y. Zhang, Z. Jin, Z. Peng, C. Liu, S. Chen, J. Ge, W. Xing, *ACS Catal.* **2016**, *6*, 6335.
- [10] Y. Li, M. Gong, Y. Liang, J. Feng, J.-E. Kim, H. Wang, G. Hong, B. Zhang, H. Dai, *Nat. Commun.* **2013**, *4*, 1805.
- [11] D. U. Lee, J. Y. Choi, K. Feng, H. W. Park, Z. Chen, *Adv. Energy Mater.* **2014**, *4*, 1301389.
- [12] J. Zhu, M. Xiao, G. Li, S. Li, J. Zhang, G. Liu, L. Ma, T. Wu, J. Lu, A. Yu, D. Su, H. Jin, S. Wang, Z. Chen, *Adv. Energy Mater.* **2020**, *10*, 1903003.
- [13] Z. Chen, A. Yu, D. Higgins, H. Li, H. Wang, Z. Chen, *Nano Lett.* **2012**, *12*, 1946.
- [14] X. Kong, K. Xu, C. Zhang, J. Dai, S. Norooz Oliaee, L. Li, X. Zeng, C. Wu, Z. Peng, *ACS Catal.* **2016**, *6*, 1487.
- [15] T. Reier, M. Oezaslan, P. Strasser, *ACS Catal.* **2012**, *2*, 1765.
- [16] J. Greeley, I. Stephens, A. Bondarenko, T. P. Johansson, H. A. Hansen, T. Jaramillo, J. Rossmeisl, I. Chorkendorff, J. K. Nørskov, *Nat. Chem.* **2009**, *1*, 552.
- [17] X. F. Yang, A. Q. Wang, B. T. Qiao, J. Li, J. Y. Liu, T. Zhang, *Acc. Chem. Res.* **2013**, *46*, 1740.
- [18] B. T. Qiao, A. Q. Wang, X. F. Yang, L. F. Allard, Z. Jiang, Y. T. Cui, J. Y. Liu, J. Li, T. Zhang, *Nat. Chem.* **2011**, *3*, 634.
- [19] S. Yang, J. Kim, Y. J. Tak, A. Soon, H. Lee, *Angew. Chem., Int. Ed.* **2016**, *55*, 2058.
- [20] H. Zhang, G. Liu, L. Shi, J. Ye, *Adv. Energy Mater.* **2018**, *8*, 1701343.
- [21] L. Yang, L. Shi, D. Wang, Y. L. Lv, D. P. Cao, *Nano Energy* **2018**, *50*, 691.
- [22] Y. Chen, S. Ji, Y. Wang, J. Dong, W. Chen, Z. Li, R. Shen, L. Zheng, Z. Zhuang, D. Wang, Y. Li, *Angew. Chem., Int. Ed.* **2017**, *56*, 6937.
- [23] M. Xiao, H. Zhang, Y. Chen, J. Zhu, L. Gao, Z. Jin, J. Ge, Z. Jiang, S. Chen, C. Liu, *Nano Energy* **2018**, *46*, 396.
- [24] M. Xiao, L. Gao, Y. Wang, X. Wang, J. Zhu, Z. Jin, C. Liu, H. Chen, G. Li, J. Ge, *J. Am. Chem. Soc.* **2019**, *141*, 19800.
- [25] C. Z. Zhu, Q. R. Shi, B. Z. Xu, S. F. Fu, G. Wan, C. Yang, S. Y. Yao, J. H. Song, H. Zhou, D. Du, S. P. Beckman, D. Su, Y. H. Lin, *Adv. Energy Mater.* **2018**, *8*, 1801956.
- [26] Z. P. Zhang, J. T. Sun, F. Wang, L. M. Dai, *Angew. Chem., Int. Ed.* **2018**, *57*, 9038.
- [27] J. Li, M. Chen, D. A. Cullen, S. Hwang, M. Wang, B. Li, K. Liu, S. Karakalos, M. Lucero, H. Zhang, *Nat. Catal.* **2018**, *1*, 935.
- [28] F. Li, G.-F. Han, H.-J. Noh, S.-J. Kim, Y. Lu, H. Y. Jeong, Z. Fu, J.-B. Baek, *Energy Environ. Sci.* **2018**, *11*, 2263.
- [29] P. Song, M. Luo, X. Liu, W. Xing, W. Xu, Z. Jiang, L. Gu, *Adv. Funct. Mater.* **2017**, *27*, 1700802.
- [30] H. Fei, J. Dong, Y. Feng, C. S. Allen, C. Wan, B. Voloskiy, M. Li, Z. Zhao, Y. Wang, H. Sun, *Nat. Catal.* **2018**, *1*, 63.
- [31] K. Liu, G. Wu, G. Wang, *J. Phys. Chem. C* **2017**, *121*, 11319.
- [32] X. Lu, C. Zhao, *J. Mater. Chem. A* **2013**, *1*, 12053.
- [33] X.-X. Ma, X.-Q. He, T. Asefa, *Electrochim. Acta* **2017**, *257*, 40.
- [34] K. Marntani, D. Jain, D. Dogu, V. Gustin, S. Gunduz, A. C. Co, U. S. Ozkan, *Appl. Catal., B* **2018**, *220*, 88.
- [35] M. Jiao, W. Song, K. Li, Y. Wang, Z. Wu, *J. Phys. Chem. C* **2016**, *120*, 8804.
- [36] C. Hu, Y. Xiao, Y. Zou, L. Dai, *Electrochim. Energy Rev.* **2018**, *1*, 84.
- [37] W. Li, C. Min, F. Tan, Z. Li, B. Zhang, R. Si, M. Xu, W. Liu, L. Zhou, Q. Wei, Y. Zhang, X. Yang, *ACS Nano* **2019**, *13*, 3177.
- [38] Z. Liang, X. Fan, H. Lei, J. Qi, Y. Li, J. Gao, M. Huo, H. Yuan, W. Zhang, H. Lin, *Angew. Chem.* **2018**, *130*, 13371.
- [39] C. Cheng, S. Li, Y. Xia, L. Ma, C. Nie, C. Roth, A. Thomas, R. Haag, *Adv. Mater.* **2018**, *30*, 1802669.
- [40] Z. Li, Z. Zhuang, F. Lv, H. Zhu, L. Zhou, M. Luo, J. Zhu, Z. Lang, S. Feng, W. Chen, L. Mai, S. Guo, *Adv. Mater.* **2018**, *30*, 1803220.
- [41] H. Zhang, W. Zhou, T. Chen, B. Y. Guan, Z. Li, X. W. D. Lou, *Energy Environ. Sci.* **2018**, *11*, 1980.
- [42] P. Chen, T. Zhou, L. Xing, K. Xu, Y. Tong, H. Xie, L. Zhang, W. Yan, W. Chu, C. Wu, Y. Xie, *Angew. Chem., Int. Ed.* **2017**, *56*, 610.
- [43] C. Tang, B. Wang, H.-F. Wang, Q. Zhang, *Adv. Mater.* **2017**, *29*, 1703185.
- [44] L. Ma, S. Chen, Z. Pei, Y. Huang, G. Liang, F. Mo, Q. Yang, J. Su, Y. Gao, J. A. Zaprien, C. Zhi, *ACS Nano* **2018**, *12*, 1949.
- [45] Y. Guo, P. Yuan, J. Zhang, Y. Hu, I. S. Armiiniu, X. Wang, J. Zhou, H. Xia, Z. Song, Q. Xu, S. Mu, *ACS Nano* **2018**, *12*, 1894.
- [46] J. Han, X. Meng, L. Lu, J. Bian, Z. Li, C. Sun, *Adv. Funct. Mater.* **2019**, *29*, 1808872.
- [47] B.-Q. Li, C.-X. Zhao, S. Chen, J.-N. Liu, X. Chen, L. Song, Q. Zhang, *Adv. Mater.* **2019**, *31*, 1900592.
- [48] C. H. Choi, C. Baldizzone, J.-P. Grote, A. K. Schuppert, F. Jaouen, K. J. J. Mayrhofer, *Angew. Chem., Int. Ed.* **2015**, *54*, 12753.
- [49] I. Martinaiou, A. H. A. Monteverde Videla, N. Weidler, M. Kübler, W. D. Z. Wallace, S. Paul, S. Wagner, A. Shahraei, R. W. Stark, S. Specchia, U. I. Kramm, *Appl. Catal., B* **2020**, *262*, 118217.